Received: 00 Month 0000 | Revised: 00 Month 0000 | Accepted: 00 Month 0000

DOI: xxx/xxxx

ARTICLE TYPE

Numerical calculation of permeability of periodic porous materials: application to periodic arrays of spheres and 3D scaffold microstructures

C. Daish*[1,2] | R. Blanchard[2] | E. Pirogova[1] | D.J.E. Harvie[3] | P. Pivonka[2,4]

[1]Discipline of Electrical and Biomedical Engineering, RMIT University, VIC 3000, Australia
[2]St Vincent's Department of Surgery, The University of Melbourne, VIC 3065, Australia
[3]Department of Chemical and Biomolecular Engineering, The University of Melbourne, VIC 3010, Australia
[4]School of Chemistry, Physics and Mechanical Engineering, Queensland University of Technology, QLD 4000, Australia

Correspondence
*Christian Daish, Discipline of Electrical and Biomedical Engineering, RMIT University, VIC 3000, Australia Email: christian.daish@gmail.com

Abstract

In this paper an efficient numerical method is proposed to calculate the anisotropic permeability in porous materials characterized by a periodic microstructure. This method is based on pore-scale fluid dynamic simulations using a static Volume of Fluid method. Unlike standard solution procedures for this type of problem, we here solve an average constitutive equation over both fluid and solid domain by use of a subgrid model to accurately capture momentum transfer from the fluid to solid interface regions. Using numerical simulations on periodic arrays of spheres, we first demonstrate that by using the subgrid interface model, more accurate results can be produced, for the velocity and pressure fields, than via more conventional approaches. We then apply numerical upscaling over the unit cell, in order to calculate the full anisotropic permeability from the pore-scale numerical results. The obtained permeability values for a variety of periodic arrays of spheres in different arrangements and packing orders are in good agreement with semi-analytical results reported in literature. This validation allows for the permeability assessment of more complex structures such as isotropic gyroid structures, or anisotropic cases, here modeled in their simplest form, the ellipsoidal inclusion.

KEYWORDS:
pore-scale, fluid dynamics, volume of fluid method, anisotropic permeability, spherical inclusions, gyroid structure

1 | INTRODUCTION

Permeability as a material property plays a significant role in many fields including applied mathematics, geological-, geotechnical-, and biomedical engineering [1; 2]. It is a parameter that measures quantitatively the ability of a porous medium to conduct fluid flow. The theory of fluid flow in many scientific fields including geophysics, soil physics, petroleum engineering and industrial chemistry, has been researched extensively [3]. In recent years, with the increased availability of sophisticated imaging technologies to assess pore structure, there has been a large increase in the use of pore-scale modeling to study flow phenomena in porous materials [4]. In biomedical engineering, a small number of studies have utilized this type of fluid modeling [5; 6; 7]. In the present study, we develop a methodology that models the fluid flow through a variety of pore morphologies in a highly efficient manner. We validate the method using geometries based on analytical descriptions of the fluid-solid interface region. We note that this method can also be applied to any natural and/or additive manufactured materials (e.g. 3D scaffolds)

where the pore microstructure is obtained using micro computed tomography (microCT) imaging [7]. In this earlier work, our team used this methodology to accurately determine the permeability characteristics of these morphologies as an aid to the extended design and development of biomaterials that most accurately represent the fluid mechanical characteristics of trabecular bone.

In tissue engineering, a biomaterial scaffold refers to a porous three-dimensional manufactured structure developed from a bio-compatible material that acts as a template for biological tissue formation [8]. Scaffold permeability is a key parameter that best represents geometrical properties such as pore shape and size, pore interconnectivity and specific surface area. Effective permeability has been suggested as a parameter to characterize scaffold mass transport properties for vascularization and bone ingrowth. Accurate prediction of an optimal permeability is a useful scaffold design tool and can assist in designing the scaffold architecture [6; 5; 9].

It is known that for slow (Low-Reynolds-number, i.e., Stokes) to moderate flow fields in porous materials, Darcy's law can be rigorously derived by volume averaging the Stokes' equation which is valid at the pore-scale [10; 11]. The most classical problem of low-Reynolds-number flow is that around a rigid sphere placed in what would otherwise be a uniform flow [12]. In order to solve the closure problem exhibited when applying volume averaging of the Stokes' equation around a particle, a number of studies have applied the theory of Stokes' flow to periodic arrays of spheres with various packing configurations [13; 11]. Although solutions to slow flow through periodic structures are often limited to conditions of small solid volume fraction [14], a number of studies have developed semi-analytical solutions to this slow flow problem around single particles [14; 15]. One aim of employing this approach to multi-particle systems is to develop averaged expressions describing mean quantities such as bulk permeability [14]. We are using the extensive knowledge of this problem to validate our method.

In order to estimate permeability of more complex structures, a number of computational models have been developed to characterize fluid flow at the pore scale [16; 6; 5]. 3D pore geometry studies most widely use the Lattice Boltzmann method or classical Computational Fluid Dynamics (CFD) [17], with most bone-specific computational models being based on the Stokes'equation [18; 19]. The Fast Fourier Transform homogenization technique has also successfully been applied to arrays of cylinders and spheres [20; 21]. The most commonly used numerical techniques are the Finite Element Method (FEM) and the Finite Volume Methods (FVM) [19; 22].

While both finite element and finite volume methods can be readily applied to unstructured meshes, the FVM is arguably the most popular method for the solution of transport equations such as the Stokes' equation. Central to the FVM is the use of Gauss' theorem to perform conservation of transported quantities around individual mesh elements. The technique is both efficient and robust, and can be used (e.g.) to model flow in complex 3D geometries [23; 24]. Within the FVM framework, two separate techniques can be applied to handle multiphase flows. The first technique uses a single mesh that contains both solid and fluid regions, but 'captures' the interface using methods such as the Immersed Boundary Method (IBM), Volume of Fluid (VOF) method and the level set method [23; 25; 26]. The second technique involves creation of a body-fitted mesh that covers only the fluid region, with simulations only performed in this region [27]. Both these types of techniques can be used for deforming (e.g. liquid/liquid) or stationary interfaces (e.g. liquid/solid), however the second technique is more commonly employed for the stationary case (e.g. solid/solid).

In the present study, we innovatively use the VOF technique for a stationary case. We chose to apply static VOF concepts within a FVM approach to model flow through a variety of pore microstructures including spherical particles, ellipsoidal particles and gyroid microstructures. Permeability analysis for the case of spherical particles will serve as validation step for our numerical method. Investigation of gyroid microstructures will be discussed with respect to bone tissue engineering applications with the perspective of more complex boundary problems (multi-scale material's architecture, drug diffusion problems, degradation of scaffold materials, etc.).

2 | METHODOLOGY

In this section we first discuss the numerical method that has been used to solve the fluid-flow problem at the pore-scale, within the multi physics finite volume solver software package **arb** [28]. We then discuss the various periodic structures (i.e., solid inclusions) that we will analyze throughout the paper. Finally, we will discuss the numerical-upscaling approach to determine the unit cell anisotropic permeability and its corresponding principal directions and eigenvalues.

2.1 | Numerical solution of fluid flow through porous materials

2.1.1 | Governing equations

We assume the case of an incompressible, single phase and slow flow, characterized by low Reynolds numbers. Therefore, flow within the pore space (fluid region) is governed by the Stokes' equations [1],

$$\boldsymbol{\nabla} \cdot \boldsymbol{u} = \boldsymbol{0} \text{ and } -\nabla p - \boldsymbol{s} = \nabla \cdot \tau \text{ on } \Omega_{\mathrm{f}} \tag{1}$$

while within the solid/fluid interface, and the solid region,

$$\boldsymbol{u} = \boldsymbol{0} \text{ on } \Gamma \text{ and } \Omega_{\mathrm{s}} \tag{2}$$

Here p is the microscopic pressure field, μ the dynamic viscosity of the fluid, $\boldsymbol{u}$ is the microscale velocity field, $\tau = -\mu\left[\nabla \boldsymbol{u} + (\nabla \boldsymbol{u})^{\mathrm{T}}\right]$ the viscous stress tensor and $\boldsymbol{s}$ the imposed pressure gradient (discussed later). Here Γ, Ω_{f} and Ω_{s} represent the solid/fluid interface, and the fluid and solid regions respectively.

2.1.2 | Numerical approximation

One method for solving equations (1) and (2) is to discretise the computational domain into unstructured computational elements such that each element contains only fluid, with the entire boundary of these elements lying along the solid/fluid interface Γ (i.e., a body-fitted mesh). Then, the equations (1) need only be solved within the fluid region Ω_{f}, with equations (2) being applied along Γ using standard computational fluid dynamics techniques. A difficulty with this technique is in deciding a) where the fluid/solid interface is located (possibly based on grayscale computer tomography (CT) scan values) and b) deciding how to treat small pores - i.e., how finely should they be meshed, and at what lengthscale can they be neglected? Hence, with the conventional re-meshing, body-fitted approach determining how computational cells should be allocated such that the overall permeability is accurately predicted while concurrently minimizing computational expense, is challenging.

In this study we avoid this complex unstructured mesh creation by instead capturing the solid geometry on a mesh that spans both the fluid and solid regions, and solving a single set of equations over the entire fluid region, solid region and the interface to produce the solution to equations (1) and (2). One advantage of this approach is that simulations can be performed on the same mesh (or averaged derivative) on which the solid geometry is defined (e.g. by a microCT scan). This removes a mesh averaging and/or interpolation step that is required for the body-fitted mesh approach.

To form the required equations, we first multiply the fluid equations by the local (element-specific) fluid volume fraction ϕ, yielding after application of the chain rule, the region non-specific continuity and momentum equations

$$\boldsymbol{\nabla} \cdot \phi \boldsymbol{u} = 0 \tag{3}$$

and

$$-\phi \boldsymbol{\nabla} p - \phi \boldsymbol{s} = \nabla \cdot \phi\tau - \boldsymbol{n}_{\Gamma} \cdot \tau \tag{4}$$

respectively, where $\boldsymbol{n}_{\Gamma} = \nabla\phi$ is a normal vector which is non-zero only along the solid/fluid interface Γ and has a magnitude that is characteristic of a delta function [29] (The numerical evaluation of $\boldsymbol{n}_{\Gamma}$ is discussed later). Equations (3) and (4) reduce to the fluid equations for $\phi = 1$, capture the interface conditions for $0 < \phi < 1$ and are consistent with the solid equations for $\phi = 0$, so unlike equations (1) and (2), are valid throughout the entire volume $\Omega = \Omega_{\mathrm{f}} + \Omega_{\mathrm{s}}$. However, within the strictly solid region Ω_{s}, where $\phi = 0$, they can neither be solved to yield the solution $\boldsymbol{u} = \boldsymbol{0}$, nor specify values for the (only numerically relevant) pressure field, so require modification for our region non-specific finite volume method.

Proceeding first with the continuity equation and pressure scalar: As the fluid pressure does not appear in the solid phase equations (Equation (2)), the fluid pressure is not strictly defined within the solid region. Hence, we are free to create an equation that the pressure must satisfy within the solid region, provided that we can show that the solution to this equation does not affect the physical property that we are trying to predict — that is, the bulk permeability. Specifically, we modify the non-specific continuity Equation (3) by including a Laplacian term that acts over the entire solid region, as in Equation (5):

$$\delta_{\mathrm{f}} \boldsymbol{\nabla} \cdot \widetilde{\phi} \boldsymbol{u} - \frac{\psi \Delta x}{\mu} \nabla \cdot \nabla p = 0 \text{ on } \Omega \tag{5}$$

where

$$\delta_{\mathrm{f}} = 1 \text{ if } \bar{\phi} > 10^{-4} \text{ otherwise } \delta_{\mathrm{f}} = 0 \tag{6}$$

is a function that identifies cells that contain a significant amount of fluid. Recognizing that under the finite volume method cell based divergences are expanded using Gauss' theorem, $\widetilde{\phi}$ are face averaged fluid volume fractions calculated using Volume of

Fluid (VOF) techniques. In turn, the cell averaged fluid volume fractions $\bar{\phi}$ on which δ_f are based are calculated by averaging the $\widetilde{\phi}$ values that surround each cell. Numerically this ensures that if the velocity divergence in Equation (5) contains a significantly non-zero $\widetilde{\phi}$, $\bar{\phi}$ will also be non-zero and $\delta_f = 1$.

The Laplacian introduced in Equation (5) causes the equations solved within the solid region to depend on the numerically stored 'pressure', p. The constants that multiply the Laplacian in Equation (5) have been included to ensure that this term retains its same magnitude relative to the velocity divergence as Δx is varied, consistent with the units of this equation. Here Δx is the local cell lengthscale and ψ is a 'pressure anchoring' lengthscale that is chosen to be small relative to the pore lengthscale. In practice we reduce ψ until the calculation of the permeability no longer depends on its value — in the current computations where the pore lengthscale is of the order 100 μm, we use $\psi = 10^{-5}$ μm. As ψ is small the Laplacian term in Equation (5) is numerically insignificant within the fluid region, however within the solid region where the computational cell averaged fluid volume fraction ($\bar{\phi}$) is zero (and hence $\delta_f = 0$) it ensures that the numerical pressure field varies in a smooth solenoidal manner between its surrounding (physical) fluid values. Note that this form of equation even allows computations to resolve (stationary) fluid velocities within completely isolated compartments within the solid region, in which the absolute fluid pressure is strictly ill defined for an incompressible fluid within a completely rigid container.

For the momentum equations, we also modify their phase non-specific form such that zero velocity is enforced within the solid (that is, Equation (2)), via

$$\delta_f \left[\bar{\phi}(\boldsymbol{\nabla} p + \boldsymbol{s}) + \nabla \cdot \widetilde{\phi}\tau - \bar{\boldsymbol{n}}_\Gamma \cdot \bar{\tau} \right] + (1 - \delta_f) \frac{\mu}{\Delta x^2} \boldsymbol{u} = \boldsymbol{0} \tag{7}$$

where $\bar{\boldsymbol{n}}_\Gamma$ and $\bar{\tau}$ are the cell averaged interface normal and viscous stress, respectively. Note that the velocity is multiplied by the factor $\mu/\Delta x^2$ to ensure that both the solid and fluid based components of this equation maintain similar magnitudes as Δx is varied. The interfacial stress contribution $\bar{\boldsymbol{n}}_\Gamma \cdot \bar{\tau}$ that appears in Equation (7) needs to be cognizant of the velocity field local to each solid/fluid interface in order to achieve mesh independence at the lowest possible mesh resolutions. To this end we use a sub-grid scale model to capture the local velocity based upon local VOF based interface reconstruction techniques. Specifically,

1. For each computational cell that contains an interface, the solid/fluid interface is reconstructed using VOF techniques such that
$$(\boldsymbol{x} - \bar{\boldsymbol{x}}) \cdot \hat{\boldsymbol{n}}_\phi = d \tag{8}$$
represents the location of the interface within that cell [29]. Here $\hat{\boldsymbol{n}}_\phi$ is a unit vector normal to the solid/fluid interface, directed into the solid and constructed from a smoothed ϕ field, and $\bar{\boldsymbol{x}}$ is the centroid of the computational cell.

2. For each face that borders an interface cell, VOF techniques are again used to calculate the face averaged fluid volume fractions, $\widetilde{\phi}$, based on the two adjacent cell interface reconstructions. For faces located away from the solid/fluid interface, $\widetilde{\phi}$ values are taken from the adjacent cells (i.e., $\widetilde{\phi} = 0$ or 1). Using VOF techniques to calculate $\widetilde{\phi}$ ensures compact support for the interfacial stress.

3. For all cells, the cell averaged fluid volume fractions $\bar{\phi}$ are then calculated by averaging the surrounding face averaged values, $\widetilde{\phi}$.

4. The cell centred interface normals are then calculated using a divergence of the face averaged fluid volume fractions, as $[\bar{\boldsymbol{n}}_\Gamma]_i = \nabla \cdot \boldsymbol{e}_i \widetilde{\phi}$, where $\boldsymbol{e}_i$ is the ith coordinate unit vector. Calculating this normal in this manner ensures that only cells that contain a solid/fluid interface (based on $\bar{\phi}$) receive an interfacial stress contribution. The unit vector $\hat{\boldsymbol{n}}_\Gamma = \bar{\boldsymbol{n}}_\Gamma / |\bar{\boldsymbol{n}}_\Gamma|$ is also calculated.

5. Finally, the cell centred interfacial stresses are calculated using
$$\bar{\tau} = -\mu \left[\overline{\nabla \boldsymbol{u}} + (\overline{\nabla \boldsymbol{u}})^{\mathrm{T}} \right] \text{ and } \overline{\nabla \boldsymbol{u}} = \frac{\chi}{d_{max}} \hat{\boldsymbol{n}}_\Gamma \boldsymbol{u} \tag{9}$$
where $d_{max} = d_{\mathrm{VOF}}(\phi = 0, \hat{\boldsymbol{n}} = \hat{\boldsymbol{n}}_\Gamma) - d_{\mathrm{VOF}}(\phi = \bar{\phi}, \hat{\boldsymbol{n}} = \hat{\boldsymbol{n}}_\Gamma)$ is the distance between the reconstructed interface in the cell and furthest vertex of the cell that lies within the fluid region, d_{VOF} is a VOF function that provides the d value within a cell defined by Equation (8) and based on the fluid volume fraction ϕ and local interface direction $\hat{\boldsymbol{n}}$, and χ is a lengthscale divisor. The premise behind Equation (9) is that within each cell each velocity component varies linearly with position, but that along the in-cell reconstructed interface the velocity is zero. Given that under the finite volume method $\boldsymbol{u}$ represents the average velocity within the cell, geometric arguments suggest that χ should be greater than 2, but an exact relationship for χ would be quite complex. Instead we regard this length divisor as an adjustable numerical

parameter, and adopt a value ($\chi = 4$) that gives the most accurate value for permeability at a given mesh resolution for the flow through a regular matrix of spheres - this analysis is given in Section 3.1.

For a further detailed description of the finite volume solver software package **arb**, the reader is directed to the work of Harvie et al. [28]. [1]

2.1.3 | Computational domain and boundary conditions

Our objective in this study is not only to predict the pore-scale flow through porous media, but also to upscale these results and produce averaged properties for periodic arrays of structured material. In this context, the target domain V, being the periodic structural element, is assumed to be a hexahedron aligned with the local coordinate system (x, y, z). Let $\partial V^{\xi,i}$, for $\xi = x, y, z$ and $i = 1, 2$ denote the six boundary faces of our computational domain V, as shown in Figure 1 . Three different sets of BCs have been used in the literature when upscaling such a periodic domain: *fixed*, *linear*, and *periodic*.

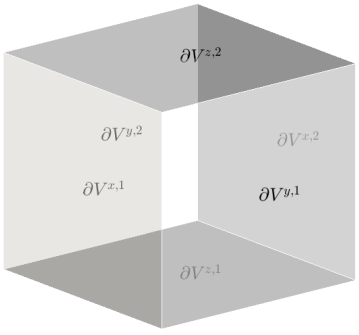

FIGURE 1 Illustration of a cubic unit cell identifying the simulation domain showing boundary faces $\partial V^{\xi,i}$ (with $\xi = x, y, z$ $i = 1, 2$)

In this study we use periodic BCs exclusively, meaning that fluid variables such as $\boldsymbol{u}$ and p are continuous across opposite faces, so that the fluid flowing out at one boundary flows into the opposite boundary. To impose periodic boundary conditions, we link opposite cells such that the computational faces on each side of the domain share values. In the employed **arb** finite volume language, this periodic mesh linking is accomplished via an in-built command applied to pairs of adjacent computational boundary faces in each of the three coordinate directions. Once the mesh is periodic, i.e., the faces are glued (**arb** terminology), then the fluid velocity on the two glued faces, in the chosen direction ξ, is the same, as is the pressure:

$$\boldsymbol{u}|_{\partial V^{\xi,1}} = \boldsymbol{u}|_{\partial V^{\xi,2}} \quad \xi = x, y, z. \tag{10}$$

$$p|_{\partial V^{\xi,2}} = p|_{\partial V^{\xi,1}} \quad \xi = x, y, z. \tag{11}$$

Due to the complete periodicity of the domain and the underlying equations, the absolute pressure value is never referenced in these simulations. Hence in order to make the numerical solution unique, we also prescribe on one computational cell boundary, a specific pressure reference value;

$$p|_{\text{one face on } \partial V} = 0. \tag{12}$$

Note that no material moves through this particular boundary due to the overall mass conservation of the FVM. As the periodicity is implemented primarily by making the mesh periodic as opposed to implementing periodicity via additional equations, there is no computational penalty in performing periodic versus non-periodic simulations, in contrast to other periodic methods [31; 32; 33]. Also boundary effects result only from the discontinuity of the solid geometry, and not to discontinuity in fluid velocities and

[1] Note that this software can be freely downloaded from http://people.eng.unimelb.edu.au/daltonh/downloads/arb/ [30].

pressure. In this study where we consider only solid geometries which either do not cross the boundary or are continuous across it, there are **no solid geometry boundary effects** and the simulation accuracy is only limited by the available mesh resolution. If the solid geometry were discontinuous across the periodic boundaries then there would be boundary effects which could be quantified by increasing the volume to surface ratio of V until this ratio no longer affects upscaled results.

2.2 | Investigated unit cells and periodic microstructures

A unit cell refers to the simplest unit of a regularly organized structure. Several studies have investigated the effect of the solid volume fraction (i.e., concentration C) of spheres in the unit cell and considered certain types of isotropic packings for which efficient computational solutions can be derived [14]. In this paper we investigate a variety of periodic structures to validate our numerical method. We first investigate three packing configurations of spherical inclusions which are typical of materials such as metals or crystals (simple cubic (SC), body-centered cubic (BCC) and face-centered cubic (FCC)). We then investigate an ellipsoidal inclusion exhibiting anisotropic flow behavior. Solutions to these problems will serve as a benchmark for the accuracy of the proposed methodology. Finally, we investigate a continuous gyroid microstructure (commonly found in 3D biomaterial scaffolds) [34].

2.2.1 | Spherical inclusions at various packing orders

Flow around rigid spherical particles (both at high and low Reynolds numbers) is one of the most studied problems in fluid dynamics [12] and a number of semi-analytical solutions have been derived for this problem. Consequently, we have chosen these type of periodic structures to benchmark the accuracy of our numerical method.

The unit cell is characterized by it's porosity Φ that varies with packing configuration and with the radius of the single spherical inclusion r, such as:

$$\begin{aligned} \Phi_{SC} &= 1 - \frac{4}{3} \cdot \pi \cdot r^3 \text{ for SC packing,} \\ \Phi_{BCC} &= 1 - 2 \cdot \frac{4}{3} \cdot \pi \cdot r^3 \text{ for BCC packing,} \\ \Phi_{FCC} &= 1 - 4 \cdot \frac{4}{3} \cdot \pi \cdot r^3 \text{ for FCC packing,} \end{aligned} \tag{13}$$

For a chosen constant particle inclusion radius r, $\Phi_{SC} \geq \Phi_{BCC} \geq \Phi_{FCC}$. We determine the spherical volumes and resultant porosities for each packing configuration based on the maximum physical inclusion diameter feasible within a unit cell of $1 \times 1 \times 1$ mm^3.

Figure 2 (left) shows a 3D representation of the respective packing orders within the unit cell of $1 \times 1 \times 1$ mm^3 and Figure 2 (right) shows the dependency of porosity on particle diameter for the three different configurations. In our calculations, for body-centered cubic and face-centered cubic packing orders, the lowest porosities (i.e., largest solid volume fraction) obtained are 0.1022 and 0.1164 for maximum diameters (2·r) of 0.95 and 0.75 mm respectively. For the simple cubic packing configuration, the lowest porosity obtained is 0.478 for a maximum inclusion diameter of 1.00 mm.

2.2.2 | Ellipsoidal inclusions with various aspect ratios

In order to test anisotropic flow within a unit cell, we incorporate ellipsoidal inclusions of varying aspect ratios (Figure 3), as it has been shown that aspect ratio has an influence on material permeability [35]. The porosity of an ellipsoidal inclusion can be calculated as the volume of the chosen unit cell minus the volume of an ellipsoid, divided by the volume of the unit cell, viz:

$$\Phi = 1 - \frac{4}{3} \cdot \pi \cdot a \cdot b \cdot c \tag{14}$$

with a, b and c being the half-lengths or radii (mm) about the z, y and x axes respectively (Figure 3 , left). In the following, we will consider $b = c$, i.e., a prolate spheroid. Figure 3 (right) shows the relationship between porosity and ellipsoidal inclusion size for four different aspect ratios (a/b). For pore-scale simulations we choose an ellipsoid with aspect ratio 1.3 and side lengths of $a = 0.498$ and $b = c = 0.380$ to achieve a porosity of 0.70.

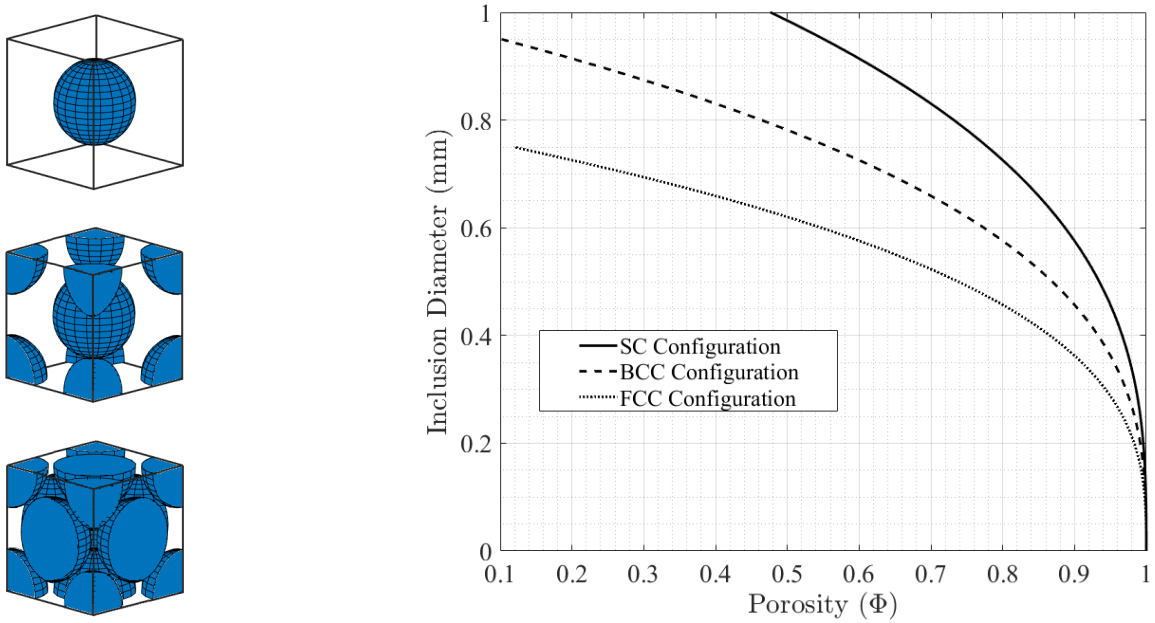

FIGURE 2 Spherical inclusions with different packing showing: (left) 3D representation of unit cells containing from top to bottom simple cubic (SC), body-centered cubic (BCC) and face-centered cubic (FCC) packing configurations, and (right) relationship between porosity (Φ) and inclusion diameter for the three packing configurations.

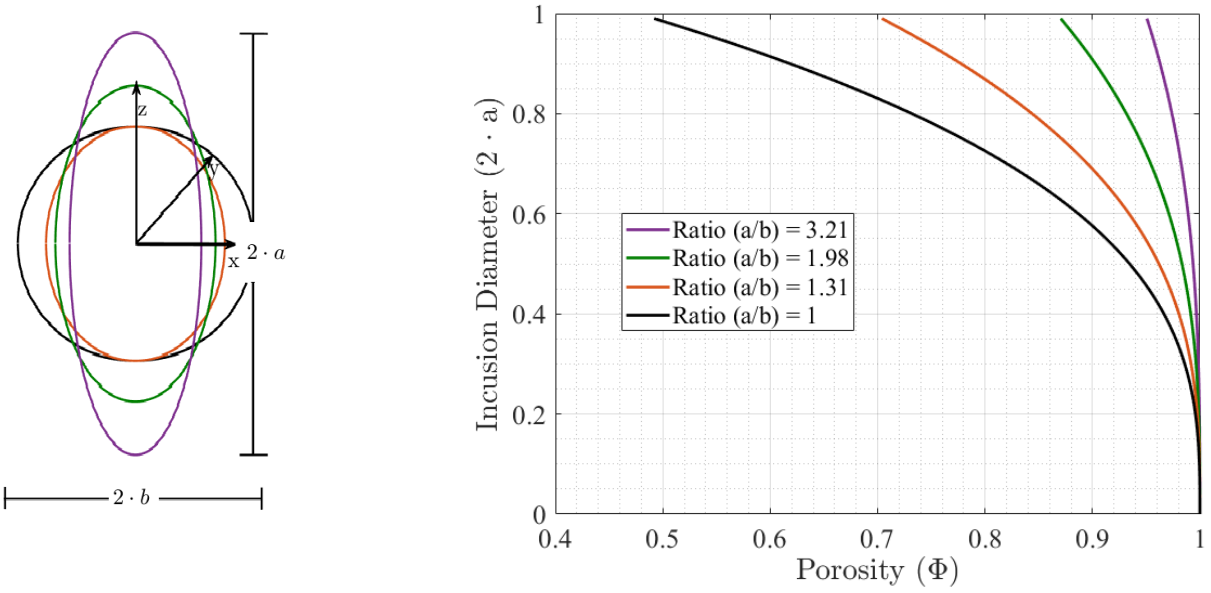

FIGURE 3 Ellipsoidal inclusion geometries showing: (left) 2D representation of ellipsoidal inclusions of four different aspect ratios (a/b; $c = b$) and (right) relationship between porosity (Φ) versus max inclusion length ($2 \cdot a$) for the different aspect ratios of ellipsoids.

2.2.3 | Gyroid microstructures for scaffold materials

The pore morphology of biological tissues, especially bone, can be approximated by interconnected periodic porous materials. Tissue engineering is a fast developing scientific field which deals with replacing damaged host tissue with materials that mimic certain properties of the host tissue, such as mechanical stiffness and strength and/or permeability. For example, in bone tissue engineering it was recently shown that the compressive strength of titanium alloy scaffolds with gyroid structures was far higher

than that of diamond and other types of pore structures with similar porosity [36]. Here we investigate the permeability behavior of 3D geometries exhibiting a gyroid microstructure.

Found in nature as intermaterial dividing surfaces the single-gyroid symmetry, consisting of circular struts and a spherical core, was first discovered in 1967 by Luzzati et al. as a cubic phase occurring in soap surfactants and in pure lipid-water systems [37; 38]. In 1970, Schoen identified the triply periodic minimal surface (TPMS) gyroid and gave a mathematical description [39].

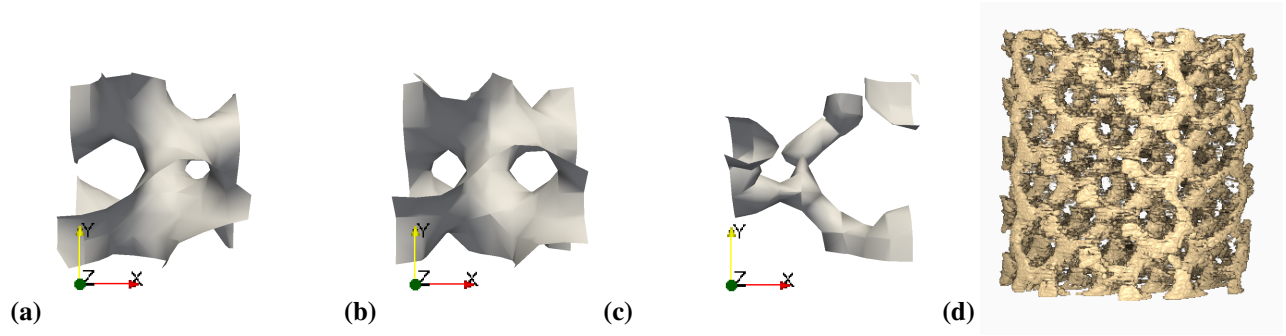

FIGURE 4 Rendering of gyroid microstructures for different strut thicknesses compared with microCT from left to right: (a) approximated gyroid with t = -0.5 and $\Phi = 0.34$, (b) approximated gyroid with t = 0.0 and $\Phi = 0.5$, (c) approximated gyroid with t = 1.3 and $\Phi = 0.94$, and (d) microCT Scanned Acrylonitrile Butadiene Styrene (ABS) specimen reconstruction with $\Phi = 0.76$.

Similarly to the work of Scherer, we approximate the single-gyroid geometry by a level surface represented by [38]:

$$sin(\frac{2\pi}{L} \cdot x)cos(\frac{2\pi}{L} \cdot y) + sin(\frac{2\pi}{L} \cdot y)cos(\frac{2\pi}{L} \cdot z) + sin(\frac{2\pi}{L} \cdot z)cos(\frac{2\pi}{L} \cdot x) = t. \quad (15)$$

where t indicates the relative strut thickness and L the side length of the unit cell used. Points $\mathbf{x} = [x, y, z]$ that satisfy Equation (15) define the surface of the gyroid geometry.

Figure 4 (a - c) shows gyroid microstructures for different values of t ranging from 0.5 to 1.3. Increasing values of t results in increases in the porosity (i.e., a decrease in solid volume fraction). For values of $t \geq 1.413$, the gyroid structure becomes disconnected [38]. Equation (15) can also be used in 3D printing to generate scaffold materials. It is important to note that when the structure becomes disconnected/discontinuous, it is no longer an applicable structure for scaffold materials. Figure 4 (d) shows a 3D rendering of a microCT image of an Acrylonitrile Butadiene Styrene (ABS) gyroid scaffold reconstructed by our group (unpublished data).

Based on the chosen size of our unit cell, $L = 1$ mm, we investigate four different cases for t in order to generate various porosity values as shown in Figure 4 . We additionally investigate a gyroid for the case $t = 0.63$ giving a porosity value of 0.7, for comparison with the spherical inclusions.

2.2.4 | Mesh generation

With continuing improvements in additive manufacturing and 3D printing technologies, the possibilities to create materials with different pore microstructures are endless. A large set of pore microstructures including the cases analysed in this paper (i.e., spheres, ellipsoids and gyroids) can all be represented by (semi) analytical formulas describing a smooth solid-fluid interface. For these cases accuracy of any fluid dynamical method strongly depends on the mesh resolution of this interfacial region.

We note that in the case of natural and/or manufactured materials this interfacial region can, in most cases, only by assessed using high-resolution microCT techniques. For the latter cases the accuracy of any fluid dynamical method is dependent on how well the chosen mesh resembles the resolution of the microCT data. In this study we used only uniform and structured meshes. On these, periodic inclusion geometries as defined by volume fraction fields were constructed using VOF shape routines that are included within the **arb** package. Representative geometries are discussed in Section 2.1, 2.2 and 2.3. Example geometries are shown in Figure 5 .

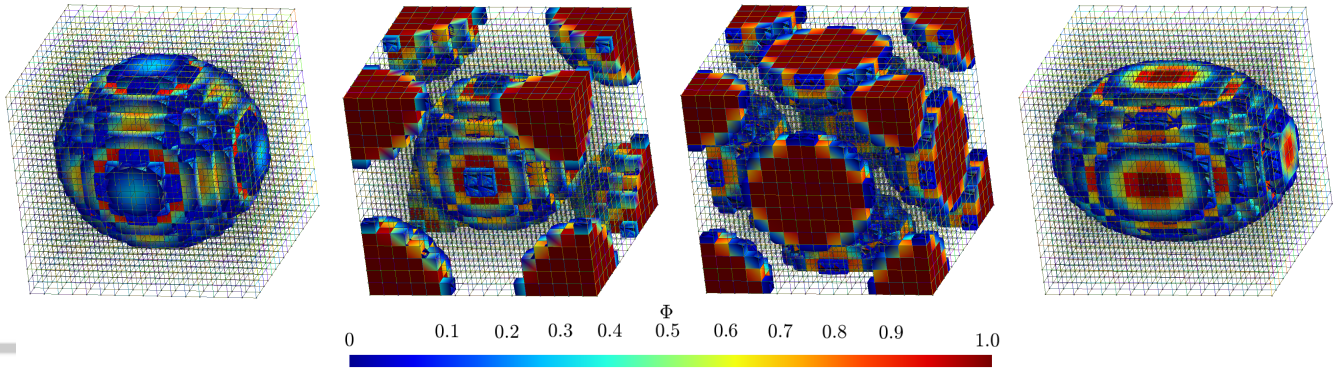

FIGURE 5 3D structured mesh generation on unit cells containing different pore microstructures from left to right: sphere with simple cubic configuration, sphere with body-centered cubic configuration, sphere face-centered cubic and ellipsoidal inclusion (cubic unit cell length: $L = 1$ mm; tetrahedral element size $= 6.25 \cdot 10^{-5}$ m; number of elements = 4,096, Φ is the local cell solid volume fraction).

2.3 | Numerical upscaling

Under certain physical conditions the complex microstructural properties of a material can be well represented by so-called effective material properties [40]. Upscaling of microscale properties such as velocity and pressure fields, in the context of Stokes' flow in porous materials, has been extensively studied however few studies have applied computational modelling in this respect [41; 40; 42].

2.3.1 | Darcy's Law

For the case of slow fluid flow in the pore space, it can be shown that volume averaging of the Stokes' momentum equation over a suitable chosen unit cell leads to the well-known Darcy's law [1; 10; 11]:

$$\mathbf{U} = -\frac{1}{\mu}\mathbf{k} \cdot \langle \nabla P \rangle \tag{16}$$

where $\mathbf{U}$ is the average fluid velocity (also denoted as Darcy velocity), $\mathbf{k}$ the intrinsic permeability tensor and $\langle \nabla P \rangle$ the average pressure gradient within the unit cell. In a real porous medium, the pressure value would decrease continuously in the direction of fluid flow. In our periodic cell approach however, this is not possible as via Equation (11), the pressure on one side of the domain equals that on the opposite face. To represent the effect of an average pressure gradient on the flow through the periodic porous medium, we introduce a large scale average pressure body force, $\boldsymbol{s}$, which appears in our constitutive equations alongside the pore-scale pressure gradient, ∇p (see equations (1) - (7)). Here we show how this averaged pressure gradient and averaged fluid velocity can be used to calculate the upscaled permeability.

Within our unit cell, the total pressure gradient ∇P can be decomposed into a local pressure variation ∇p and our imposed pressure gradient, $\boldsymbol{s}$ as:

$$\nabla P = \nabla p + \boldsymbol{s}, \tag{17}$$

Volume averaging ($\langle\rangle$) of equation (17) gives:

$$\langle \nabla P \rangle = \langle \nabla p \rangle + \langle \boldsymbol{s} \rangle \tag{18}$$

But as $\boldsymbol{s}$ is uniform, $\langle \boldsymbol{s} \rangle = \boldsymbol{s}$. Further examining the local pressure variation, noting that the domain is periodic, gives:

$$\begin{aligned}
\langle \nabla p \rangle &= \frac{1}{|V|} \int_V \nabla p \, dV \\
&= \frac{1}{|V|} \sum_{\zeta=x,y,z} \left\{ \int_{\partial V^{\zeta,1}} -\mathbf{e}_\zeta p dA + \int_{\partial V^{\zeta,2}} \mathbf{e}_\zeta p dA \right\} \\
&= \frac{1}{|V|} \sum_{\zeta=x,y,z} \left\{ -\mathbf{e}_\zeta \left[\int_{\partial V^{\zeta,1}} p dA - \int_{\partial V^{\zeta,2}} p dA \right] \right\} = 0 \\
\therefore \langle \nabla P \rangle &= \boldsymbol{s}
\end{aligned} \tag{19}$$

where $\mathbf{e}$ represents a unit vector with directions $\zeta = i, j, k$. Note that $[\int_{\partial_V^{\xi,1}} p dA - \int_{\partial_V^{\xi,2}} p dA] = 0$ follows from Equation (11). Similarly for velocity:

$$\mathbf{U} = \langle \boldsymbol{u} \rangle = \frac{1}{|V|} \int_V \boldsymbol{u} \, dV, \tag{20}$$

where $\boldsymbol{u}$ is the pore-scale velocity field obtained from solving the Stokes' equation (3) and V includes both Solid and Fluid regions, i.e., the entire computational domain. Inserting of equations (18) and (19) into Equation (16) leads to:

$$\mathbf{U} = -\frac{1}{\mu} \mathbf{k} \cdot \boldsymbol{s} \tag{21}$$

Hence, to find $\mathbf{k}$ from a simulation result of known $\boldsymbol{s}$, we calculate $\mathbf{U}$ based on Equation (20) and then invert Equation (21). If we know the relationship between $\boldsymbol{s}$ and $\mathbf{U}$ for three different directions of $\boldsymbol{s}$, it can be shown that $\mathbf{k}$ is a symmetric second order tensor (i.e., 3×3 matrix) with real coefficients (k_{ij}) which reflects the anisotropy of the pore-scale flow [22; 43; 44], i.e.,

$$\mathbf{k} = \begin{pmatrix} k_{xx} & k_{xy} & k_{xz} \\ \vdots & k_{yy} & k_{yz} \\ sym & \cdots & k_{zz} \end{pmatrix}. \tag{22}$$

Since the matrix $\mathbf{k}$ has nine unknowns, we can solve a linear system of equations with three chosen orthogonal vectors. Given that flow follows Stokes' regime, $\mathbf{k}$ is independent of the magnitude of $\boldsymbol{s}$, so for the simulations we use unit pressure gradients in the x, y and z directions. This delivers a system of equations relating ($\mathbf{U}_\eta$) to $\tilde{k}_{ij}$, with $\tilde{k}_{ij}$ being the macroscopic permeability coefficient for directions i, j and μ the viscosity of the fluid, in our case water, i.e., $\mu = 0.001$ Pa·s [44]. Solving these equations for each of the enforced pressure gradient terms (direction η) gives the permeability tensor. In general, due to numerical resolution inaccuracies this matrix is slightly non-symmetrical and can be symmetrized by taking the average for the cross terms.

2.3.2 | Principal components of k

Based on the finite-dimensional spectral theorem [45], any symmetric tensor/matrix whose entries are real can be diagonalized by an orthogonal matrix $\mathbf{Q}$. Consequently $\mathbf{k}$ can be diagonalized as:

$$\mathbf{k}^p = \mathbf{Q}^T \cdot \mathbf{k} \cdot \mathbf{Q} = \begin{pmatrix} k_1^p & 0 & 0 \\ \vdots & k_2^p & 0 \\ sym & \cdots & k_3^p \end{pmatrix}. \tag{23}$$

where k_i^p ($i = 1, 2, 3$) are the three eigenvalues of $\mathbf{k}$, while $\mathbf{Q}$ is composed of the orthogonal basis of eigenvectors of $\mathbf{k}$ and $\mathbf{Q}^T$ is the transpose of $\mathbf{Q}$. Geometrically $\mathbf{Q}$ represents a rotation matrix and $\mathbf{k}^p$ represents a transformation of $\mathbf{k}$ into principal coordinates. Common practice is to set the i subscript values 1, 2 and 3 of $\mathbf{k}^p$ to maximum (k_{max}^p), intermediate (k_{int}^p) and minimum (k_{min}^p) respectively. Here

$$\mathbf{Q} = [\mathbf{e}_{k_1}, \mathbf{e}_{k_2}, \mathbf{e}_{k_3}]. \tag{24}$$

where $\mathbf{e}_{k_1}$,$\mathbf{e}_{k_2}$ and $\mathbf{e}_{k_3}$ are the eigenvectors of $\mathbf{k}$. In the context of permeability, values for k_i^p are generally different from each other indicating that the sample is not isotropic, but rather orthotropic. For this study, the MATLAB function eig(E,D) was used to determine the eigenvalues and eigenvectors of $\mathbf{k}$.

2.3.3 | Characterizing anisotropy

Anisotropy of permeability is of great importance in geological-, industrial- and bio-engineering. Three subtypes of material anisotropy can be distinguished based on the number of independent coefficients in the permeability tensor however for this study we take into account only two subtypes: (i) isotropic and (ii) transversely isotropic (or polar anisotropic) materials.

- Isotropic materials are characterized by an infinite number of planes of symmetry and, hence, can be described with a single independent constant of permeability ($k_{xx} = k_{yy} = k_{zz}, k_{ij} = 0 \quad \text{for} \quad i \neq j$).
- Transversely isotropic materials have physical properties which are symmetric about an axis that is normal to a plane of isotropy. Such materials can be described by two independent constants ($k_{xx}, k_{yy} = k_{zz}, k_{ij} = 0 \quad \text{for} \quad i \neq j$).

Anisotropy can be evaluated using the anisotropic ratio R defined as [46]:

$$R = \frac{k_{min}^p}{\sqrt{k_{int}^p \cdot k_{max}^p}}. \tag{25}$$

R values equal to 1 characterize isotropic flow behavior, while R values lower than 1 characterize anisotropic flow behaviour. There are degrees of anisotropy however and values less than 0.8 are generally used to indicate significantly anisotropic flows.

3 | RESULTS

In this section we present the results of our study in terms of optimal parameters to be used in the numerical simulations, i.e., choice of lengthscale divisor χ and mesh resolution. We also look at convergence of the numerical results for all different packing orders and pore morphologies. Finally, we upscale the converged solutions to calculate the permeability matrices. Note that for all numerical simulations we assumed that water was the fluid flowing through the porous material, i.e., a viscosity of 0.001 Pa·s was used.

3.1 | Choice of lengthscale divisor χ and mesh resolution

The lengthscale divisor introduced in Equation (9) has an optimal value, giving the most accurate results for a given mesh resolution. Note that for an infinitely fine mesh, the value of χ would be immaterial, and indeed, a non-VOF treatment with $\bar{\tau} = 0$ could be used. Figure 6 shows the convergence of permeability for a spherical inclusion of SC configuration and a gyroidal inclusion, comparing χ values from 1 to ∞ ($\bar{\tau} = 0$) as a function of mesh resolution. In Figure 6 we note that the permeability decreases for both inclusions as the mesh resolution increases, except for the case where $\chi = \infty$ wherein permeability in fact increases with an increase in mesh resolution. Whilst there is a certain degree of variation between $\chi = 1$ and $\chi = 8$ for meshes $\leq 10,000$ elements (78% and 73% variation for gyroids and spheres respectively), the difference in permeability becomes small (19% and 18% variation respectively) for meshes $\geq 100,000$ elements. As the calculated permeability at low mesh resolutions and $\chi = 4$ most accurately represents the calculated permeability at high mesh resolutions, we employed a χ value of 4 for further determination of permeability in this study.

Also shown in Figure 6 are the results of additional finite volume simulations, also conducted using the **arb** package [28], but performed using a more conventional body fitted unstructured mesh. The meshes used were composed of both tetrahedrons away from the sphere, and hexahedrons surrounding the sphere, in order to most efficiently resolve the velocity gradients close to the sphere surface. Periodic boundary conditions were again applied. Examination of the results shows that the permeability of the SC array of spheres again converges to a value of around $1.1 \cdot 10^{-8}$ m^2 as the mesh is refined, consistent with our VOF based approach (which was conducted on a uniform and structured mesh). Comparison of the two techniques may suggest that the body-fitted approach is slightly more accurate than the VOF based uniform mesh approach for a given number of cells, however this comparison is somewhat misleading: the memory usage and computational solution time of the body-fitted approach tends

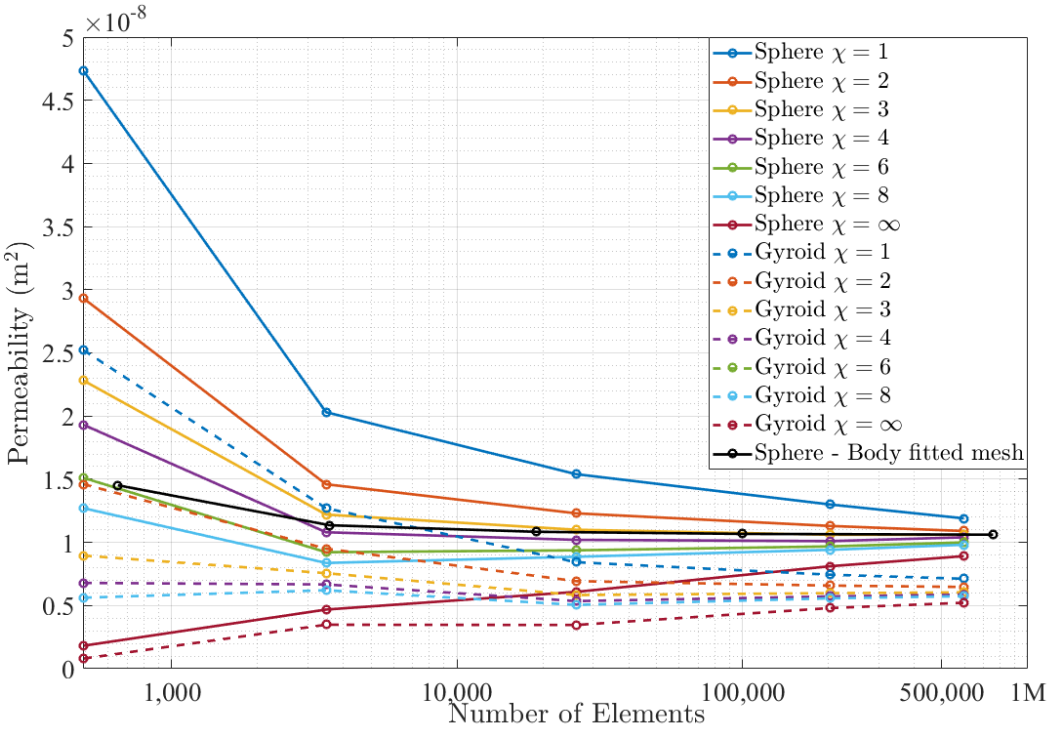

FIGURE 6 Convergence of permeability with changing χ values for a sphere of simple cubic configuration both singular and as an array, and a gyroid of $t = 0.63$, both with porosity of 70%. Also shown is the case in which $\bar{\tau} = 0$, i.e., $\chi = \infty$. For all cases the pressure gradient magnitude is 1.0 and results are shown for the z direction outputs, i.e., k_3^p.

to be larger and longer, respectively, than the VOF based uniform mesh approach, for the same number of cells. This is because both the accuracy and computational efficiency of a uniform and structured mesh is generally higher than an unstructured mesh that has the same number of elements. Also note, that while it is relatively easy to construct a body-fitted mesh that surrounds a single sphere as used in this validation example, body-fitted mesh generation for more complex (i.e., CT scan based) geometries is more difficult, as discussed previously. Hence the motivation for detailing and validating our new VOF based uniform mesh approach.

Figure 7 shows the output from running simulations on a unit cell comprising a spherical inclusion of each packing configuration, an ellipsoidal inclusion and a gyroid geometry, at a variety of mesh resolutions. For all simulations, the pressure gradient applied is of magnitude 1 and the results shown are for the z direction, i.e., k_3^p. It should be noted however that results are independent of this value. A lengthscale divisor of $\chi = 4$ was used. As indicated, adequate convergence of permeability is achieved at around $40,000$ elements for each of the spherical inclusions and the gyroid, while convergence is achieved for the ellipsoidal inclusion at approximately $200,000$ elements. Importantly, results are seen to converge as the mesh is refined (i.e., more elements).

For subsequent simulations on structured meshes, a mesh size of 38,912 elements was used for the spherical inclusions, whilst a mesh size of 202,859 elements was used for the ellipsoidal and gyroid inclusions. These values represent an acceptable compromise between simulation accuracy and computational expense.

3.2 | Computation of permeability for different microstructures

3.2.1 | Isotropic configurations

Table 1 shows the bulk permeabilities for each of the spherical packing configurations for a uniform porosity of 0.70. Although porosity is the same in all cases, the permeability changes depending on packing order. Permeability decreases as the sizes of the spheres decreases (which is the case from SC to BCC to FCC), i.e., resistance to fluid flow increases. For each packing order, due to the periodicity of the inclusion applied, flow is isotropic. The gyroid permeability is also isotropic (due to the triply periodic microstructure) and is similar to the spherical inclusion with BCC configuration.

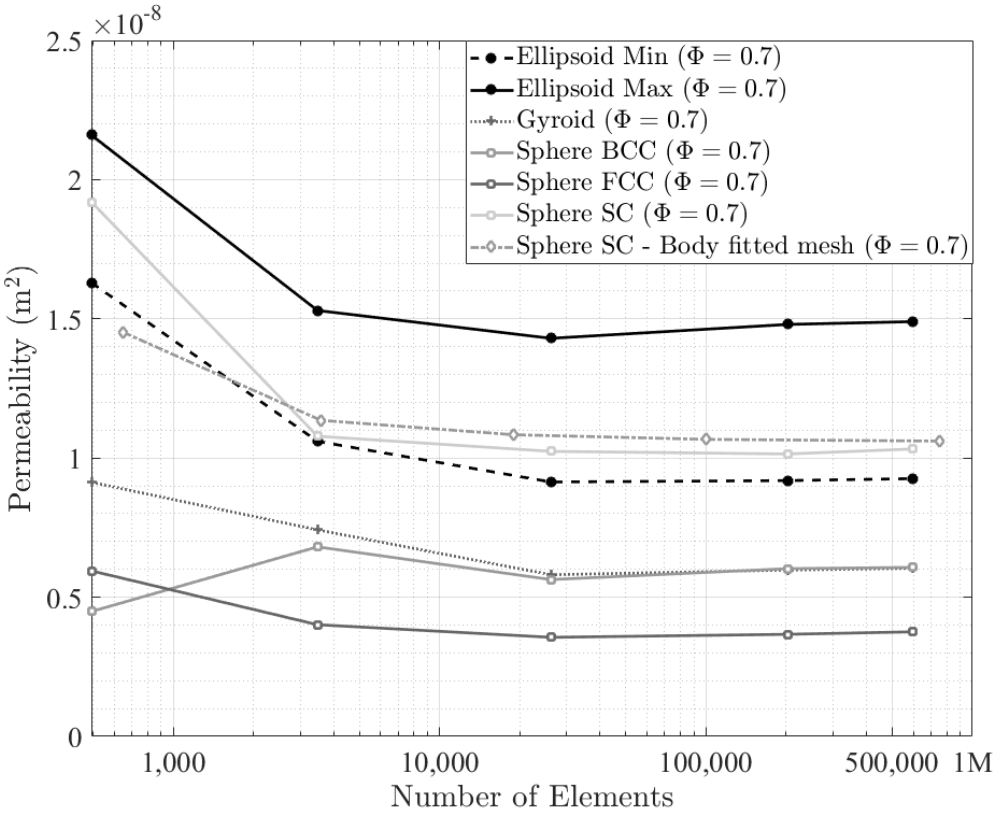

FIGURE 7 Results following simulations of each geometry type, refining the mesh resolution in order to reach a converged solution for $\chi = 4$. In order to achieve a porosity of 70%, the radii for each configuration SC, BCC and FCC are respectively 0.415, 0.3296 and 0.2616 mm; the dimension a for the ellipsoid is 0.498 mm, with an aspect ratio of 1.31 with the pressure gradient in the z direction, i.e., k_3^p; and the value of t is 0.69 for the gyroid.

3.2.2 | Anisotropic configuration - ellipsoidal inclusion

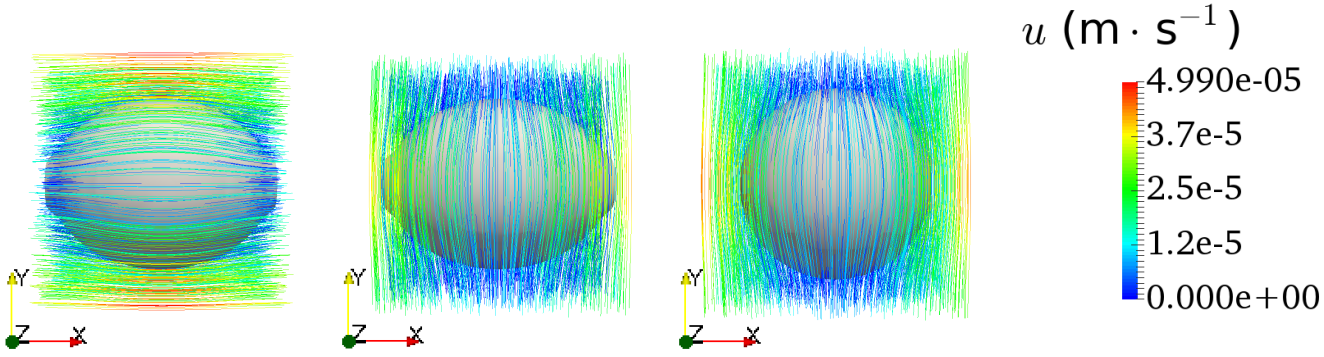

FIGURE 8 Velocity streamline profile output following **arb** pore-scale simulations on an ellipsoid of aspect ratio 1.31 and a simple cubic spherical inclusion , showing from left to right, ellipsoidal inclusion for unit pressure gradient $\boldsymbol{s_1}$, ellipsoidal inclusion for unit pressure gradient $\boldsymbol{s_2}$, simple cubic spherical inclusion for unit pressure gradient $\boldsymbol{s_2}$ and streamline distribution colour map.

Whilst the flow around spherical inclusions is isotropic, for an ellipsoidal inclusion, the flow is generally anisotropic and depends on the aspect ratio. In the present case, the long axis of the ellipsoid is aligned with the direction x. The dimensions of the other ellipsoid axis are kept equal, i.e., b=c. As shown in Table 2 , the permeability in the k^p_3 (i.e., x-axis) direction is greater than that in the $k^p_{1,2}$ directions. This result is further investigated in Figure 8 comparing the velocity streamline profiles around a simple spherical inclusion and the ellipsoidal inclusion, with both unit cells having the same porosity of $\Phi = 0.7$.

In Figure 8 we observe a maximum velocity vector component of $4.99 \cdot 10^{-5}$ m·s^{-1} following an applied pressure gradient in the x-direction (i.e., $\boldsymbol{s_1}$) on the domain surrounding the ellipsoidal inclusion. This maximum component is larger than the maximum vector component surrounding the spherical inclusion ($4.42 \cdot 10^{-5}$ m·s^{-1}) following an equivalent pressure gradient in the same $\boldsymbol{s_1}$ direction. Applying an equal pressure gradient in the y-direction however (as in Figure 8 (second from the left)) results in a maximum vector component of only $4.17 \cdot 10^{-5}$ m·s^{-1}, which is not only less than that in the x-direction, but also less than that of the spherical inclusion. These higher and lower pore-scale velocities present in the ellipsoidal inclusion, despite both geometries having the same porosity ($\Phi = 0.7$), are due to the fact that whilst the pressure gradient is the same, shorter and longer side lengths respectively decrease and increase hindrance of flow. Similarly, the upscaled Darcy velocity in the x-direction ($\mathbf{U}_{s_1}$ ($1.50 \cdot 10^{-5}$ m·s^{-1})) is larger for the ellipsoidal case compared with that of the spherical inclusion ($1.13 \cdot 10^{-5}$ m·s^{-1}) in the same direction. This results in anisotropic permeability for the ellipsoidal inclusion. Comparing upscaled permeability results (simple cubic inclusion from Table 1 and column two in Table 2), we observe that $k^p_{3_{ellipsoid}} \geq k^p_{1,2,3_{sphere}} \geq k^p_{1,2_{ellipsoid}}$. The upscaled principal permeability values for the ellipsoidal inclusions clearly signify this anisotropy (i.e., $k^p_1 = k^p_2 \neq k^p_3$). Based on Equation (25) the anisotropic ratios $\boldsymbol{R}$ found for each ellipsoid suggest significant anisotropy.

3.2.3 | Gyroid microstructures

Following numerical upscaling detailed in Section 2.3, and diagonalization of the full symmetric upscaled permeability tensor $\mathbf{k}$, the principal permeability tensor $\mathbf{k}^p$ is obtained and presented for two ellipsoidal inclusions, and for the four gyroid microstructures (see Table 2). For the ellipsoid, the porosity was fixed at 0.70 however for the gyroids porosity ranges from 0.34 to 0.99 were investigated. Permeability values range from 0.85 to $59.2 \cdot 10^{-9}$ m^2. There is a clear trend in this case showing that permeability increases with an increase in porosity. Also shown in Table 2 are the values for anisotropic ratio $\boldsymbol{R}$ (see Equation (25)).

The gyroids show perfect isotropy (within the simulation accuracy). In verifying the isotropy of the gyroids, we also conducted simulations with varying pressure gradient $\mathbf{s}$ directions that were not aligned with the coordinate directions. At the low resolution (i.e., lower computational accuracy) in which these simulations were performed, off diagonal permeabilities varied from zero by a maximum of $0.02 \cdot 10^{-9}$ m^2. Principal permeability values for the different orientations of pressure gradients differed slightly due to numerical inaccuracy. Hence, within the limits of numerical accuracy, our $\mathbf{k}$ tensor is independent of the $\boldsymbol{s}$ directions chosen.

4 | DISCUSSION

In this study, we successfully and efficiently compute fluid properties in two scales: the pore velocity and pressure quantities at the pore-scale and the permeability tensor at the material scale. Whilst we do not present results taken directly from CT scan data, we present accurate results from structures that have been defined by data which is equivalent to CT scan data.

In Figure 9 we compare our results with data extracted from a number of semi-analytical and experimental studies relating the permeability of packed spherical inclusions to a unit cell porosity [13; 14; 47]. We approximate our findings by relating particle size with permeability based on the Blake-Kozeny correlation [13]:

$$\frac{k(1-\Phi)^2}{d_p^2\Phi^3} = \frac{1}{180} \tag{26}$$

where Φ refers to the porosity, and d_p the effective particle diameter (2·r). This correlation relates the permeability to the spherical inclusion geometric properties (including porosity) for all packing concentrations.

The y-axis in Figure 9 represents the dimensionless permeability, scaled according to Equation (26), i.e., the Blake-Kozeny relation [13]. As can be observed, results obtained from our numerical simulations (dashed lines connecting the discrete simulation results indicated by crosses) are in good agreement with those found in the literature for all three packing orders (BCC (red

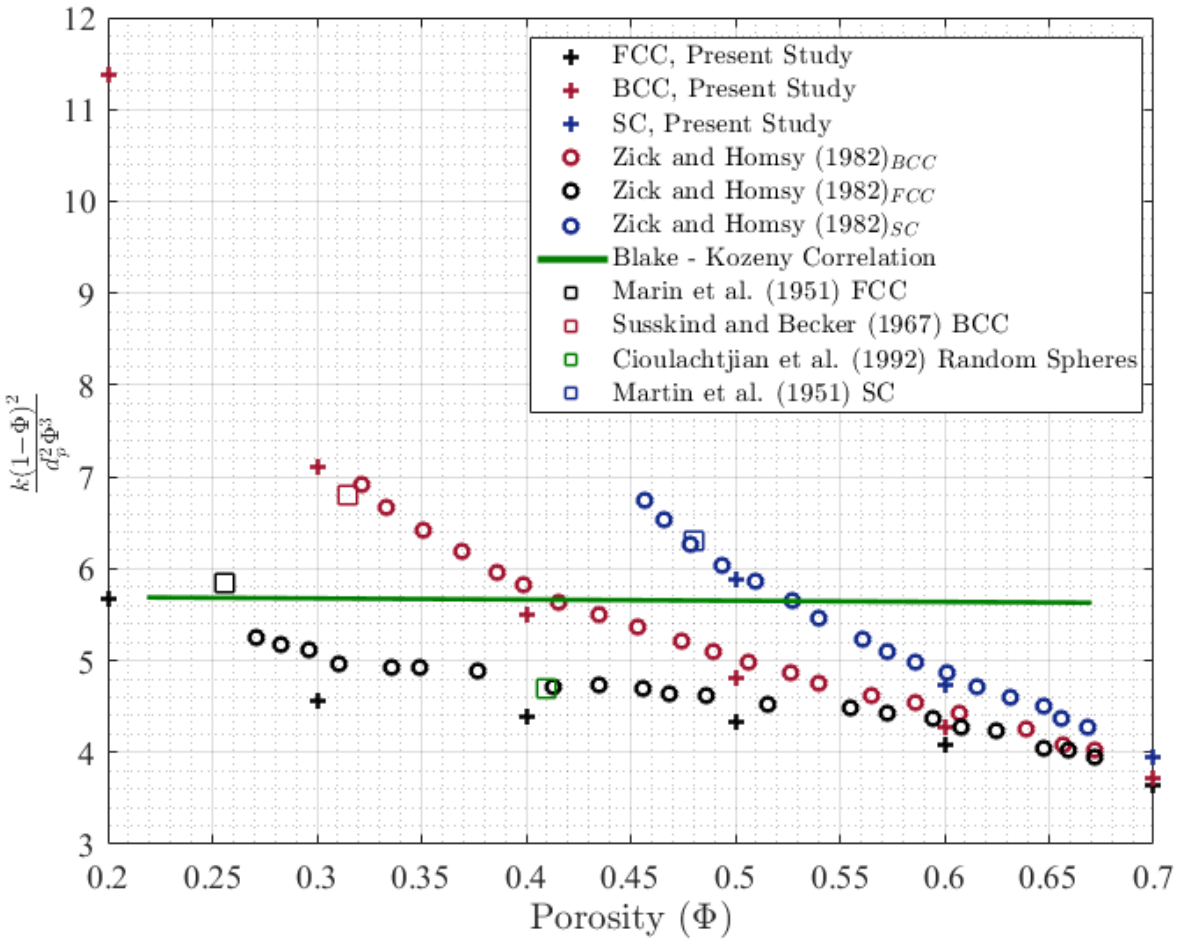

FIGURE 9 Comparison of various semi-analytical results and experimental data with the current numerical method, porosity (Φ) versus dimensionless permeability ($\frac{k(1-\Phi)^2}{d_p^2\Phi^3}$) showing simulation results from the present study for each packing order comparing with results extracted from data of Zick and Homsy, Martin et al., Susskin and Becker, and Cioulachtjian et al [14; 48; 47; 49].

dashed circle), SC (blue dashed circle), FCC (black dashed circle). Note the k values used to evaluate the dimensionless permeability (left side of Equation (26)) are upscaled permeabilities determined through the methodology proposed in this paper. Comparison suggests that our solutions closely match experimental studies [47; 48; 49]. These findings offer a good validation for our VOF method in isotropic cases.

Following the extension of Einstein's spherical reasoning to the case of particles of ellipsoidal shape [50], many have looked to address the problem of slow flow past ellipsoids with several studies presenting semi-analytical formulas and results further stipulating the importance of particle orientation and degree of non-sphericity/ellipticity [51; 52]. In our study, we show the importance of particle orientation by varying ellipsoidal aspect ratios (a/b) and observing the influence on anisotropic ratio and final permeability.

Mathematically and from Equation (25), any value of R less than 1 is considered anisotropic and $R = 1$ for isotropic materials. As mentioned previously however, there are several degrees of anisotropy. When taking into account an ellipsoidal inclusion, it is important to note that the anisotropic ratio R is dependent on the longitudinal and transverse side lengths. In Figure 10 we show how the longitudinal and transverse lengths (a and b respectively) affect the final anisotropy. In order to compare the flow problem with ellipsoidal inclusions to our previously investigated cases of spherical inclusions, we keep the porosity constant, i.e., $\Phi = 0.7$. Based on this porosity constraint we vary the aspect ratio of the ellipsoid, i.e., a/b (with $c = b$). This allows calculation of a and b. As can be seen in Figure 10 (left) due to the constraint on porosity, the values of a and b reach extreme

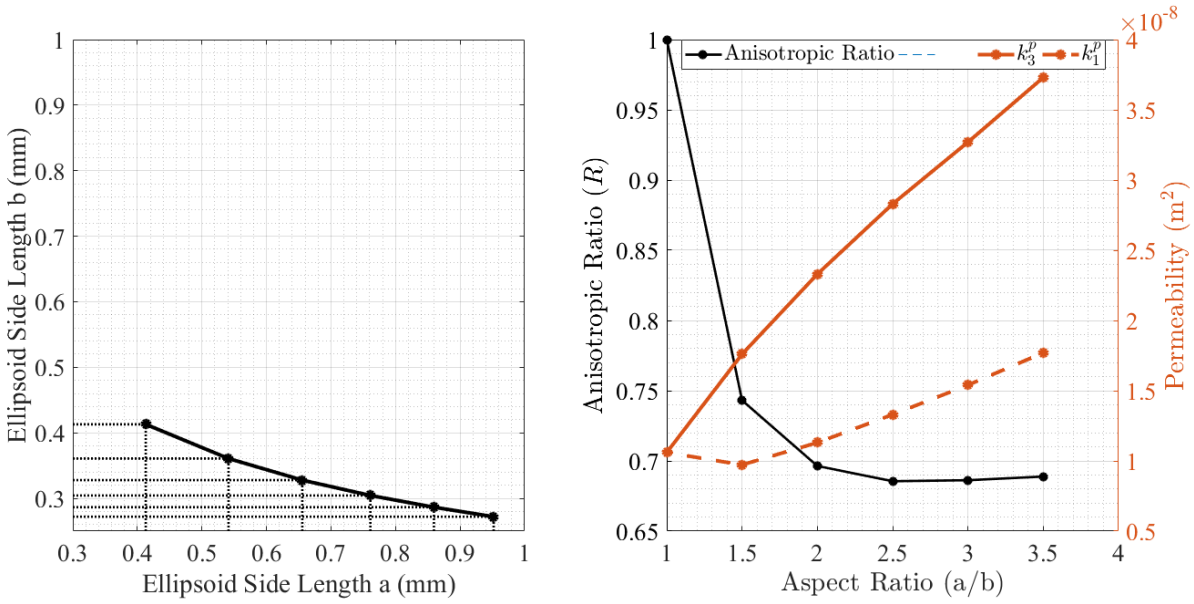

FIGURE 10 Comparison of ellipsoidal geometries showing (left) contrast of ellipsoidal side half-lengths (a & b) for a fixed porosity (Φ) of 0.7 with discrete lines at aspect ratio values between 1.0 and 3.5, (right) comparison of anisotropic ratio vs aspect ratio (a/b) with no fixed porosity for aspect ratio values between 1.0 and 3.5 in increments of 0.5. k_3^p and k_1^p permeability values at each aspect ratio are also included.

values of $a = b = 0.41$ mm ($a/b = 1$) and $a = 0.952; b = 0.27$ ($a/b = 3.5$). Figure 10 (right) shows the decrease of the anisotropic value R from an initial value 1 ($a/b = 1$ isotropic case) to a value of around 0.68 for an aspect ratio of $a/b = 2.5$. Similarly, permeability shows a dependence on aspect ratio. When the eigenvalues are the same, i.e., $k_3^p = k_1^p$, we get an initial anisotropic ratio of $R = 1$. Then we observe that k_3^p starts to increase significantly while k_1^p decreases resulting in a decrease in R. Both k_3^p and k_1^p then begin to increase at an aspect ratio of $a/b = 2$. Due to the fact that $\sqrt{k_1^p}/\sqrt{k_3^p}$ remains constant, one can conclude that for $a/b \geq 2$, R also remains approximately constant, i.e., $R = 0.68$.

The permeabilities we calculated for the gyroid structures are consistent with values reported in the literature. In the context of evaluating tissue engineered scaffold structures, Ali and Sen, Dias et al. measured real scaffold permeabilities in the ranges of $9.09{\cdot}10^{-9}$ to $2.7{\cdot}10^{-8}$, and $4{\cdot}10^{-9}$ m^2 respectively both for porosities of 70.0% [6; 53]. Similarly, Melchels, Barradas et al. measured the permeability of the same single gyroid structure considered here (i.e., defined by Equation 15) [54]. Their specific structure had a measured porosity of 67.5±3.8%, and permeability non-dimensionalised by the specific surface area (a form of Darcy number) in the range 0.043 to 0.0519. Our simulations of this same structure [2], but having a porosity of 70% gave a corresponding Darcy number of 0.051. This value is near the upper end of the range measured by Melchels et al., consistent with the porosity of our simulated material being slightly higher than that of the experimentally measured material.

We summarise our single-gyroid results by two curve fits. The relationship between porosity Φ and strut thickness t is found to be linear, obeying:

$$\Phi = 0.33t + 0.5 \tag{27}$$

Also, using the periodic side length L of 1 mm employed in our simulations, based on our five values for k we have found the approximate relationship:

$$k = 0.0023 \cdot \frac{\Phi}{1-\Phi} \cdot L^2 \tag{28}$$

Figures 11 and 12 show these two functions in the Supplementary material.

[2]To calculate the specific surface area (per total volume) from the simulations, we integrate the VOF delta function over the computational domain using $S = \int_V |\bar{n}_\Gamma| dV / V$

where V is the volume of the computational domain

Other groups have calculated gyroid permeabilities via simulation. Jung and Torquato used an Immersed Boundary Finite Volume Method to find the permeability of the same single gyroid structure having a 50% porosity, as $2.2889{\cdot}10^{-3}$ (here non-dimensionalised by the structure periodic length) [32]. Our equivalent value is $2.4 \cdot 10^{-3}$ (Table 2, $t = 0$), which is just 4.5% larger, despite being calculated with an order of magnitude less computational elements (202,859 elements in our study vs 2,146,689 elements used by Jung and Torquato). As Jung and Torquato do not present a mesh resolution study for this particular geometry, we cannot speculate on the reason for the small difference between results, but note that our mesh resolution study for the 70% porosity gyroid showed only a 0.99% difference in permeability when increasing mesh count from 202,859 to 596,851 elements (see Figure 7). Broadly this supports our assertion that the presented VOF-based FVM is able to resolve the macro-scale permeability of a porous material very economically - that is, with the minimum amount of computational memory. This economy will be paramount in predicting the permeabilities of real porous structures that are not generally periodic, and hence require large representative sample surface to volume ratios in order to minimize boundary effects (see Section 2.1.3).

Our reported gyroid permeabilities are also consistent with the permeabilities calculated for similar geometries, even though direct comparisons are not possible. For example, Bobbert et al. used multiphysics software and the falling head experimental method to determine the permeability characteristics of gyroid structures with porosities between 0.52 and 0.66, achieving permeability results of 1.29 to $6.96{\cdot}10^{-9}$ m^2 [55]. Our own results for porosities between 50% and 70% similarly range from 0.8 to $6.1{\cdot}10^{-9}$ m^2.

In regards to engineering periodic biomaterial scaffolds, Triply perioidic minimal surfaces (TMPS) (such as the Schwarz diamond (D) and the Schoen gyroid (G)) that can be designed computationally and developed through rapid prototyping (RP) are now being utilized more commonly [33]. It has been found through several studies that gyroids are better for cell seeding, are more permeable due to the lack of size-limiting pore interconnections, have a more open and accessible pore network, and provide a better accessibility of fluid compared to other structures such as hexagons [54; 56; 31]. It has also been shown that whilst gyroid structures are isometric architectures, by varying the porosity distributions longitudinally or radially, it is possible to create an anisotropic structure [56].

Calculation of fluid flow in porous materials is generally computationally intensive due to the required size of the volume of interest (VOI) which is in the order of millimeters compared to the size of the pore diameters which are in the order of hundreds of micrometers [7; 6]. Computational domain size varies depending on the achievable numerical resolution, but most sizes reported in the literature range between $1 \times 1 \times 1$ mm^3 and $5 \times 5 \times 5$ mm^3 [22; 44]. Convergence of numerical results is not commonly reported. The numerical results found in the literature vary with imaging resolution and computational capacity, however are within a comparable range to experimental findings [56; 54; 5].

In the present study, simulations were performed on an ***Intel*** *Xeon CPU E5-2650 v2* at 2.60 GHz having 16 physical cores. Computing at $\chi = 4$ took three minutes for spherical inclusions at 38,912 elements, and 20 minutes for each gyroid inclusion at 202,859 elements. This was substantially less time (15 minutes and 2.5 hours respectively) than computing at $\chi = \infty$. Applying the VOF method in our case, proved to be highly efficient, significantly more so than without VOF, i.e., $\bar{\tau} = 0$.

5 | CONCLUSION AND OUTLOOK

In the present study, we described a comprehensive method for calculating the permeability of periodic porous materials. We first took domain geometries often represented in literature to validate the method. As these first geometries are discontinuous, we then applied the method to a commonly found continuous biomaterial scaffold geometry. No studies have been able to concisely characterize flow through periodic structures at the pore-scale using VOF techniques to take into account momentum transfer exhibited in multiphase flow. We demonstrated an efficient and accurate technique for calculating pore-scale fluid flow properties, inclusively on large meshes ($\geq 1M$ elements). The importance of this method is that it is able to accurately predict the flow around periodic elements and through porous structures, where the elements/structures are defined solely by data which is equivalent to CT scan data - i.e., mesh-cell averaged volume fractions. Our upscaled permeability outcomes match well with semi-analytical and experimental results reported in the literature, as well as with additional simulations conducted using a more conventional body-fitted mesh approach.

Based on numerical simulation results, we showed that a lengthscale divisor of $\chi = 4$ (a numerical modelling parameter introduced in the method) produces the most accurate results for a given mesh resolution, however as the number of mesh cells increases (>100,000 for our examples) the divisor then only has a marginal influence on the results. In terms of convergence, for spherical, ellipsoidal and gyroidal inclusions, a mesh size of at least 40,000 elements is required to produce an accurate result.

With large meshes, simulations were run efficiently without overt computational expense. Despite applying the same pressure gradient $\boldsymbol{s}$ for all inclusions, the spherical inclusions were fully isotropic, the ellipsoidal inclusion was anisotropic and each of the gyroid inclusions (regardless of strut thickness t) were isotropic also. Hence, the chosen $\boldsymbol{s}$ does not affect the final anisotropy.

To conclude, we believe that the developed method can effectively be applied in various scientific fields including geotechnical engineering, chemical engineering and bioengineering. Particularly, for the latter application, the method can be used to rapidly estimate three dimensional permeability of scaffold materials to be used for bone replacement applications.

ACKNOWLEDGEMENTS

The authors are grateful to the Australian Research Council (ARC) for the financial support through the discovery project [DP 120101680]. Professor Pivonka and Mr. Daish acknowledge the support of this work by the Australian-German collaboration award (UA-DAAD Joint Research Cooperation Scheme). This research is supported by RMIT University, through the SECE Top Up Scholarship.

References

1. Bear J, Bachmat Y. *Introduction to Modeling of Transport Phenomena in Porous Media*. Theory and Applications of Transport in Porous MediaDordrecht, The Netherlands: Kluwer Academic Publishers; 1990.
2. Adler PM. *Porous Media: Geometry and Transport*. Stoneham: Butterworth-Heineman; 1994.
3. Collins RE. *Flow of Fluids through Porous Materials*. Petroleum Publishing Co., Tulsa, OK; 1976.
4. Blunt MJ. Flow in porous media-pore-network models and multiphase flow. *Current Opinion In Colloid & Interface Science.* 2001;6(3):197–207.
5. Truscello S, Kerckhofs G, Van Bael S, Pyka G, Schrooten J, Van Oosterwyck H. Prediction of permeability of regular scaffolds for skeletal tissue engineering: a combined computational and experimental study. *Acta Biomaterialia.* 2012;8(4):1648–1658.
6. Dias MR, Fernandes PR, Guedes JM, Hollister SJ. Permeability analysis of scaffolds for bone tissue engineering. *Journal of Biomechanics.* 2012;45(6):938–944.
7. Daish C, Blanchard R, Gulati K, et al. Estimation of anisotropic permeability in trabecular bone based on microCT imaging and pore-scale fluid dynamics simulations. *Bone Reports.* 2017;6:129–139.
8. Langer R, Tirrell DA. Designing materials for biology and medicine. *Nature.* 2004;428(6982):487–492.
9. Li E, Chang CC, Zhang Z, Li Q. Characterization of tissue scaffolds for time-dependent biotransport criteria–a novel computational procedure. *Computer Methods in Biomechanics and Biomedical Engineering.* 2016;19(11):1210–1224.
10. Whitaker S. Flow in porous media I: A theoretical derivation of Darcy's law. *Transport in Porous Media.* 1986;1(1):3–25.
11. Quintard M, Whitaker S. Transport in ordered and disordered porous media: volume-averaged equations, closure problems, and comparison with experiment. *Chemical Engineering Science.* 1993;48(14):2537-2564.
12. Grodzinsky A. *Field, Forces and Flows in Biological Systems*. Garland Science; 2011.
13. Barrere J, Gipouloux O, Whitaker S. On the closure problem for Darcy's law. *Transport in Porous Media.* 1992;7(3):209–222.
14. Zick AA, Homsy GM. Stokes flow through periodic arrays of spheres. *Journal of Fluid Mechanics.* 1982;115:13–26.
15. Youngren GK, Acrivos A. Stokes flow past a particle of arbitrary shape: a numerical method of solution. *Journal of Fluid Mechanics.* 1975;69(02):377–403.

16. Sanz-Herrera JA, García-Aznar JM, Doblaré M. Micro–macro numerical modelling of bone regeneration in tissue engineering. *Computer Methods in Applied Mechanics and Engineering.* 2008;197(33):3092–3107.

17. Aw MS, Khalid KA, Gulati K, et al. Characterization of drug-release kinetics in trabecular bone from titania nanotube implants. *International Journal of Nanomedicine.* 2012;7:4883-4892.

18. Widmer RP, Ferguson SJ. A comparison and verification of computational methods to determine the permeability of vertebral trabecular bone. *Proceedings of the Institution of Mechanical Engineers, Part H: Journal of Engineering in Medicine.* 2013;:0954411912462814.

19. Teo JCM, Teoh SH. Permeability study of vertebral cancellous bone using micro-computational fluid dynamics. *Computer Methods in Biomechanics and Biomedical Engineering.* 2012;15(4):417–423.

20. To Viet-Thanh, Monchiet Vincent, To Quy Dong. An FFT method for the computation of thermal diffusivity of porous periodic media. *Acta Mechanica.* 2017;228(9):3019–3037.

21. Ly Hai Bang, Monchiet Vincent, Grande Daniel. Computation of permeability with Fast Fourier Transform from 3-D digital images of porous microstructures. *International Journal of Numerical Methods for Heat & Fluid Flow.* 2016;26(5):1328–1345.

22. Guibert M, Horgue P, Hamon G, Creux P, Debenest G. Computational permeability determination from pore-scale imaging: Sample size, mesh and method sensitivities. *Transport in Porous Media.* 2015;107(3):641–656.

23. Hirt CW, Nichols BD. Volume of fluid (VOF) method for the dynamics of free boundaries. *Journal of Computational Physics.* 1981;39(1):201–225.

24. Harvie DJE, Fletcher DF. A new volume of fluid advection algorithm: the stream scheme. *Journal of Computational Physics.* 2000;162(1):1–32.

25. Raeini AQ, Blunt MJ, Bijeljic B. Modelling two-phase at the pore scale using the volume-of-fluid method. *Journal of Computational Physics.* 2012;231(17):5653–5668.

26. Sussman M, Puckett EG. A coupled level set and volume-of-fluid method for computing 3D and axisymmetric incompressible two-phase flows. *Journal of Computational Physics.* 2000;162(2):301–337.

27. Hirt CW, Amsden AA, Cook JL. An arbitrary Lagrangian-Eulerian computing method for all flow speeds. *Journal of Computational Physics.* 1974;14(3):227–253.

28. Harvie DJE. An implicit finite volume method for arbitrary transport equations. *ANZIAM Journal.* 2012;52:1126–1145.

29. Brackbill JU, Kothe DB, Zemach C. A continuum method for modelling surface tension. *Journal of Computational Physics.* 1992;100:335–354.

30. Harvie DJE. Software: Multiphysics fluid dynamics. 2016;.

31. Boccaccio A, Ballini A, Pappalettere C, Tullo D, Cantore S, Desiate A. Finite element method (FEM), mechanobiology and biomimetic scaffolds in bone tissue engineering. *International Journal of Biological Science.* 2011;7(1):112–132.

32. Jung Y, Torquato S. Fluid permeabilities of triply periodic minimal surfaces. *Physical Review E.* 2005;72(5):056319.

33. Shin J, Kim S, Jeong D, et al. Finite element analysis of Schwarz P surface pore geometries for tissue-engineered scaffolds. *Mathematical Problems in Engineering.* 2012;2012.

34. Hasimoto H. On the periodic fundamental solutions of the Stokes equations and their application to viscous flow past a cubic array of spheres. *Journal of Fluid Mechanics.* 1959;5(02):317–328.

35. Larson RE, Higdon JJL. Microscopic flow near the surface of two-dimensional porous media. Part 1. Axial flow. *Journal of Fluid Mechanics.* 1986;166:449–472.

36. Yánez A, Herrera A, Martel O, Monopoli D, Afonso H. Compressive behaviour of gyroid lattice structures for human cancellous bone implant applications. *Materials Science and Engineering: C.* 2016;.

37. Luzzati V, Tardieu A, Gulik-Krzywicki T, Rivas E, Reiss-Husson F. Structure of the cubic phases of lipid–water systems. *Nature.* 1968;.

38. Scherer MRJ. *Double-Gyroid-Structured functional materials: synthesis and applications*. Springer Science & Business Media; 2013.

39. Schoen AH. *Infinite periodic minimal surfaces without self-intersections*. 1970.

40. Kachanov M, Sevostianov I. On quantitative characterization of microstructures and effective properties. *International Journal of Solids and Structures.* 2005;42(2):309–336.

41. Renard Ph, De Marsily G. Calculating equivalent permeability: a review. *Advances in Water Resources.* 1997;20(5):253–278.

42. Xu Wentao, Fish Jacob. A multiscale modeling of permeability in a multi-porosity porous medium using smoothed particle hydrodynamics. *International Journal for Numerical Methods in Engineering.* 2017;111(8):776–800.

43. Lei G, Dong PC, Mo SY, Yang S, Wu ZS, Gai SH. Calculation of full permeability tensor for fractured anisotropic media. *Journal of Petroleum Exploration and Production Technology.* 2015;5(2):167–176.

44. Odsæter LV. Numerical Aspects of Flow Based Local Upscaling. PhD thesisNorwegian University of Science and Technology2013.

45. Bronshtein IN, Semendyayev KA. *Handbook of Mathematics*. Springer Science & Business Media; 2013.

46. Clavaud JB, Maineult A, Zamora M, Rasolofosaon P, Schlitter C. Permeability anisotropy and its relations with porous medium structure. *Journal of Geophysical Research: Solid Earth.* 2008;113(B1).

47. Susskind H, Becker W. Pressure drop in geometrically ordered packed beds of spheres. *AIChE Journal.* 1967;13(6):1155–1159.

48. Martin JJ, McCabe WL, Monrad CC. Pressure drop through stacked spheres: Effect of orientation. *Chemical Engineering Progress.* 1951;47.

49. Cioulachtjian S, Tadrist L, Occelli R, Santini R, Pantaloni J. Experimental analysis of heat transfer with phase change in porous media crossed by a fluid flow. *Experimental thermal and fluid science.* 1992;5(4):533–547.

50. Jeffery GB. The motion of ellipsoidal particles immersed in a viscous fluid. 1922;102:161–179.

51. Loth E. Drag of non-spherical solid particles of regular and irregular shape. *Powder Technology.* 2008;182(3):342–353.

52. Brenner H. The Stokes resistance of an arbitrary particle-IV: arbitrary fields of flow. *Chemical Engineering Science.* 1964;19(10):703–727.

53. Ali Davar, Sen Sadri. Finite element analysis of mechanical behavior, permeability and fluid induced wall shear stress of high porosity scaffolds with gyroid and lattice-based architectures. *Journal of the mechanical behavior of biomedical materials.* 2017;75:262–270.

54. Melchels FPW, Barradas AMC, Van Blitterswijk CA, De Boer J, Feijen J, Grijpma DW. Effects of the architecture of tissue engineering scaffolds on cell seeding and culturing. *Acta Biomaterialia.* 2010;6(11):4208–4217.

55. Bobbert FSL. Permeability and mechanical properties of triply periodic minimal surface scaffolds for bone regeneration. Ms. ThesisDelft University of Technology2016.

56. Olivares AL, Marsal È, Planell JA, Lacroix D. Finite element study of scaffold architecture design and culture conditions for tissue engineering. *Biomaterials.* 2009;30(30):6142–6149.

SUPPLEMENTARY

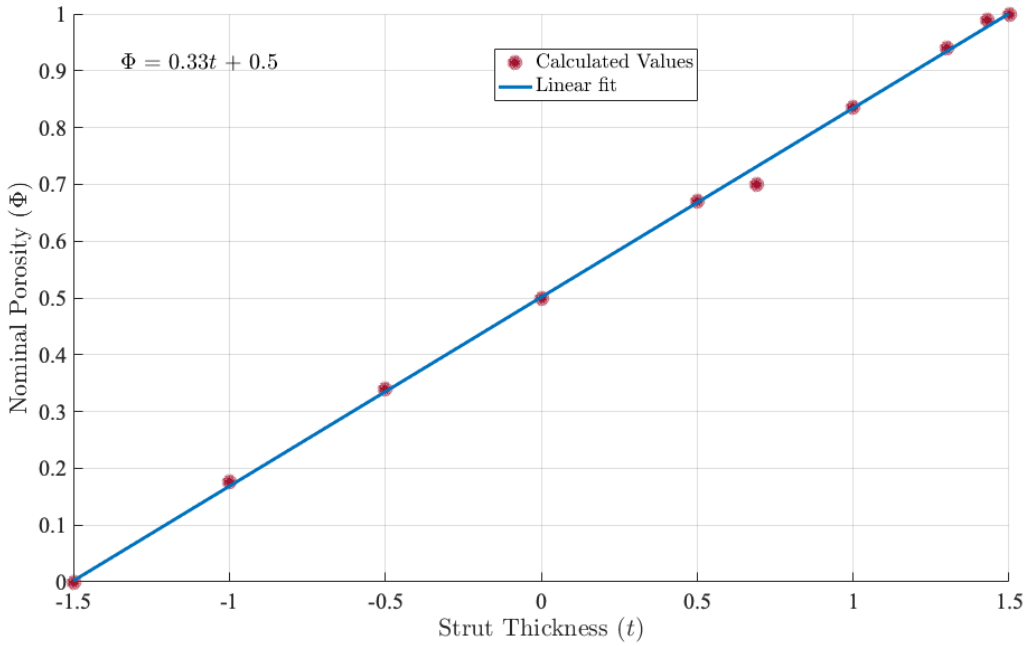

FIGURE 11 Calculated nominal porosities for Gyroids of varying strut thickness (t) showing the linearly-fitted curve and corresponding equation.

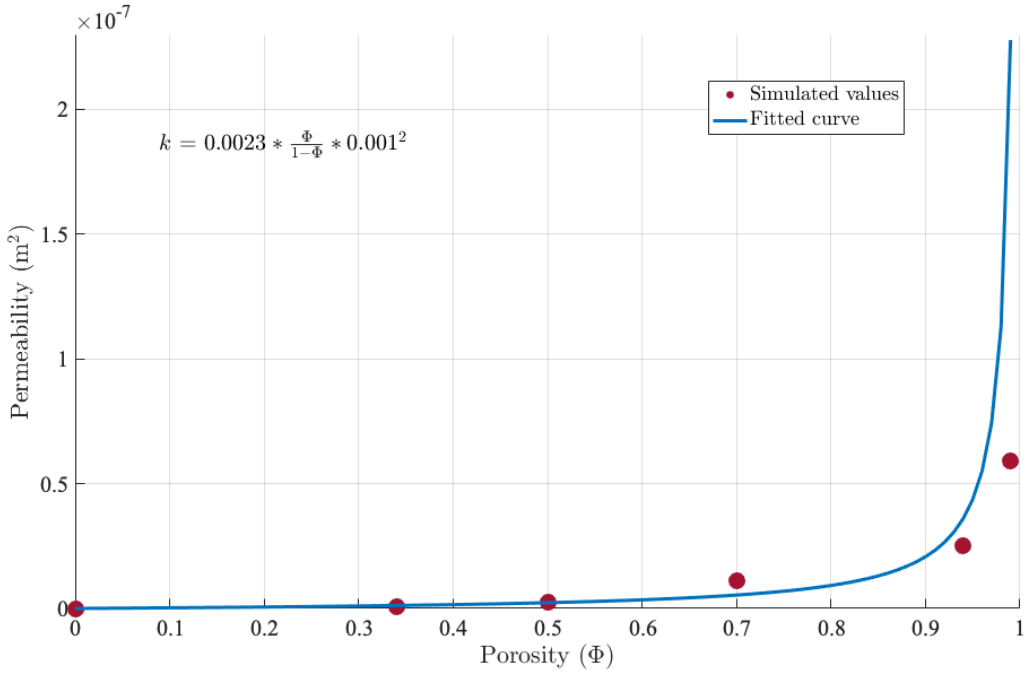

FIGURE 12 Calculated permeabilities for Gyroids of varying porosity (Φ), i.e., 0, 0.34, 0.50, 0.70, 0.94 and 0.99, showing the most representative fitted curve and corresponding equation.

TABLES

TABLE 1 Comparison of different spherical inclusion packing orders (SC, BCC and FCC) showing corresponding principal permeability (k^p), porosity (Φ) and radius of inclusion (r). Also shown is a gyroid structure of $\Phi = 0.7$ with $t = 0.63$ for comparison.

	Simple Cubic	**Body-Centered Cubic**	**Face-Centered Cubic**	**Gyroid** $t = 0.63$	**Units**
Φ	0.70	0.70	0.70	0.70	-
k_3^p	1.13	0.68	0.43	0.61	$\cdot 10^{-8}$ m^2
k_2^p	1.13	0.68	0.43	0.61	$\cdot 10^{-8}$ m^2
k_1^p	1.13	0.68	0.43	0.61	$\cdot 10^{-8}$ m^2
r	0.41	0.33	0.26	NA	mm

TABLE 2 Comparison of up-scaled permeability values determined for an ellipsoidal inclusion, with those for the gyroid inclusions

	Ellipsoid ($a/b = 1.98$, $b = c$)	**Ellipsoid** ($a/b = 1.31$, $b = c$)	**Gyroid** ($t = -0.5$)	**Gyroid** ($t = 0$)	**Gyroid** ($t = 1.3$)	**Gyroid** ($t = 1.43$)	**units**
k_3^p	2.03	1.50	0.08	0.24	2.52	5.92	$\cdot 10^{-8}$ m^2
k_2^p	0.96	0.93	0.08	0.24	2.52	5.92	$\cdot 10^{-8}$ m^2
k_1^p	0.96	0.93	0.08	0.24	2.52	5.92	$\cdot 10^{-8}$ m^2
Φ	0.67	0.70	0.34	0.50	0.94	0.99	-
R	0.69	0.79	1	1	1	1	-

NOMENCLATURE

Variables

χ	lengthscale divisor
$\boldsymbol{s}$	imposed average pressure gradient
∇	vector differential operator nabla
u	pore-scale velocity
∇p	pore-scale pressure gradient
p	pore-scale pressure
P	average pore-scale pressure
τ	viscous stress tensor
Ω	spatial domain
Ω_f	fluid region domain
Ω_s	solid region domain
Γ	solid/fluid interface
μ	viscosity of the fluid phase
ϕ	pore-scale porosity
$\mathbf{n}_\Gamma$	a normal non-zero vector

ψ	pressure anchoring lengthscale
Δ	operator
Δx	mesh dimension (side length)
δ	kronecker operator
d_{max}	distance between reconstructed interface and furthest vertex
V	whole volume of unit cell (simulation domain)
Φ	macroscale porosity
r	radius of a single sphere
d_p	spherical particle diameter
a	ellipsoid axis side half-length
b	ellipsoid axis side half-length
c	ellipsoid axis side half-length
C	solid volume fraction (1 - Φ)
L	size of the computational domain (unit cell side length)
t	gyroid strut thickness
$\mathbf{U}$	Darcy velocity
$\mathbf{k}$	intrinsic permeability tensor
∇P	macroscale pressure gradient
$\tilde{k}$	macroscopic permeability tensor
$\langle\rangle$	volume average
$\mathbf{Q}$	orthogonal rotation matrix
e_{k_i}	eigen vector
I	identity matrix
R	anisotropic ratio
v_i	velocity components of ellipsoid flow

Abbreviations

RVE	representative volume element
VOF	volume of fluid
CFD	computational fluid dynamics
FEM	finite element method
FVM	finite volume method
BC	boundary condition
FCC	Face-centred cubic
SC	Simple cubic
BCC	Body-Centred Cubic
SD	standard deviation
VOI	volume of interest

Superscripts

	face averaged
$-$	cell averaged
p	principal flow direction
T	transpose operator

Subscripts

$symm$	symmetrized
int	intermediate value of...
max	maximum value of...
min	minimum value of...

s	solid
f	fluid